J. Fluid Mech. (1991), *vol.* 232, *pp.* 629–646
Printed in Great Britain

Chaotic streamlines inside drops immersed in steady Stokes flows

By H. A. STONE[1], ALI NADIM[2] AND STEVEN H. STROGATZ[2]

[1] Division of Applied Sciences, Harvard University, Cambridge, MA 02138, USA

[2] Department of Mathematics, MIT, Cambridge, MA 02139, USA

(Received 12 December 1990)

Motivated by the recent work of Bajer & Moffatt (1990), we investigate the kinematics of bounded steady Stokes flows. Specifically, we consider the streamlines inside a neutrally buoyant spherical drop immersed in a general linear flow. The Eulerian velocity field internal to the drop, known analytically, is a cubic function of position. For a wide range of parameters the internal streamlines, hence the fluid particle paths, may wander chaotically. Typical Poincaré sections show both ordered and chaotic regions. The extent and existence of chaotic wandering is related to (i) the orientation of the vorticity vector relative to the principal axes of strain of the undisturbed flow and (ii) the magnitude of the vorticity relative to the magnitude of the rate-of-strain tensor. In the limit of small vorticity, we use the method of averaging to predict the size of the dominant island region. This yields the critical orientation of the vorticity vector at which this dominant island disappears so that particle paths fill almost the entire Poincaré section. The problem studied here appears to be one of the simplest, physically realizable, bounded steady Stokes flows which produces chaotic streamlines.

1. Introduction

In recent years the kinematics of mixing has been a topic of widespread interest in the fluid dynamics community. Emphasis has focused on the development of a detailed understanding of several prototypical flows. Examples include the flow due to two blinking vortices (Aref 1984) and the two-dimensional flow fields generated by time-periodic motion of either eccentric cylinders (Aref & Balachandar 1986), or the sidewalls of a cavity flow apparatus (Leong & Ottino 1989). Current research emphasizes the close connection of the fluid dynamical problem with the mathematics of dynamical systems theory and chaos. The reader interested in the ubiquitous character of mixing flows and chaos is referred to Ottino (1989).

The majority of papers studying the kinematics of mixing have examined two-dimensional time-periodic motions. Indeed, the Hamiltonian structure of the two-dimensional flow problem facilitates analytical and numerical study (e.g. Rom-Kedar, Leonard & Wiggins 1990), as well as a detailed comparison between experiment and theory (Swanson & Ottino 1990). However, it is also known that three-dimensional steady flows can produce chaotic particle paths; the ABC flow (Dombre *et al.* 1986), which is a steady, space-periodic velocity field satisfying the inviscid Euler equations, is perhaps the best known example. The streamlines in the ABC flow are in general unbounded and the streamline chaos appears as particle paths which sample a large region of characteristic cross-sectional planes of the flow. Two other steady flows with unbounded chaotic streamlines are the so-called

partitioned pipe mixer and the helical annular pipe mixer, which, typically, are modelled using the steady Stokes equations (Ottino 1989).

Very recently, Bajer & Moffatt (1990) gave the first example of a bounded steady three-dimensional Stokes flow with chaotic streamlines. They considered the most general quadratic velocity field inside a sphere, a mathematical problem motivated by applications in dynamo theory. Their example illustrates the (often overlooked) fact that streamlines need not be closed, even though the flow is bounded, steady, and divergence-free ($\nabla \cdot \boldsymbol{u} = 0$).

In this paper we extend the work of Bajer & Moffatt by considering the natural physical problem of a neutrally buoyant spherical drop immersed in a general linear steady Stokes flow. In this case, the external flow field is characterized by the vorticity vector and the rate-of-strain tensor. The velocity field internal to the drop is known analytically and is a cubic function of position. Using this exact solution, we demonstrate that streamlines wander chaotically inside the drop for a wide range of parameters.

It may seem surprising that this simple steady Stokes flow can produce chaotic particle paths, since, after all, Stokes equations are linear equations for the velocity field. However, here it is important to distinguish between dynamics and kinematics. The motion of a spherical drop in a steady linear flow is a dynamical problem where the velocity field depends linearly upon the external forcing, say the rate-of-strain tensor and the vorticity vector. Simultaneously, the associated kinematical problem, describing the evolution of the particle paths as a function of time, is three-dimensional and nonlinear, hence may lead to chaotic particle trajectories. It is this feature of the Stokes flow problem investigated here, i.e. linear dynamics and nonlinear kinematics, which may appear to be contradictory at first sight. However, these are really two distinct aspects of the same problem.

Perhaps most importantly, in this work the equations describing fluid particle trajectories have a very simple structure and so may prove useful in further studies of the transport characteristics internal and external to droplets in flow. A related study has already been undertaken in the context of electromagnetic stirring (Moffatt 1991). Finally, the equations introduced in this paper possess a rich dynamical structure and are therefore interesting to study in their own right.

2. The flow field

Consider the flow field due to a spherical drop, density $\hat{\rho}$, viscosity $\hat{\mu}$, suspended in a Newtonian fluid with density ρ and viscosity μ. Choose a coordinate system moving with the centre-of-mass velocity of the drop and assume that the interfacial tension is sufficiently large to maintain a spherical drop shape. Far from the drop the fluid is assumed to undergo a steady general linear motion $\boldsymbol{u}^{\infty}(\boldsymbol{x}) = \boldsymbol{U} + \frac{1}{2}\boldsymbol{\omega} \wedge \boldsymbol{x} + \boldsymbol{E} \cdot \boldsymbol{x}$, where $\boldsymbol{x}$ is the position vector measured from the centre of the drop, $\boldsymbol{\omega}$ is the vorticity vector and $\boldsymbol{E}$ is the symmetric, traceless rate-of-strain tensor of the undisturbed motion. This description of the local flow field about a drop is a good approximation for those fluid motions where the drop radius a is much smaller than the typical lengthscale characteristic of velocity gradient variations in the bulk flow. Hence, at least in principle, this model flow provides the starting point for a local description of mixing in a multiphase dispersion of droplets.

It is straightforward to solve the steady incompressible Stokes flow problem for the velocity field internal and external to a drop satisfying the boundary conditions of continuity of velocity and continuity of tangential stress. (The normal stress

balance is not imposed because the drop is assumed to have a spherical shape.) For the case of a neutrally buoyant drop ($\hat{\rho} = \rho$), which translates with the local fluid velocity $\boldsymbol{U}$ but cannot deform exactly as a fluid element, the velocity field internal to the drop is given exactly by

$$\boldsymbol{u}(\boldsymbol{x}) = \frac{1}{2(1+\lambda)}[(5r^2-3)\boldsymbol{E}\cdot\boldsymbol{x} - 2\boldsymbol{x}\boldsymbol{x}\cdot\boldsymbol{E}\cdot\boldsymbol{x}] + \tfrac{1}{2}\boldsymbol{\omega}\wedge\boldsymbol{x}. \tag{1}$$

Here all lengths have been non-dimensionalized by the drop radius a and velocities have been non-dimensionalized by Ga where G is a typical shear rate of the flow. In (1), $\lambda = \hat{\mu}/\mu$ is the viscosity ratio of the two fluids and $r^2 = \boldsymbol{x}\cdot\boldsymbol{x}$. A brief derivation of this equation is given in Appendix A.

The fluid particle paths, which coincide with the streamlines (and streaklines) for this steady flow, follow from the solution of the autonomous, volume-preserving ($\nabla\cdot\boldsymbol{u} = 0$) system of equations

$$\frac{\mathrm{d}\boldsymbol{x}}{\mathrm{d}t} = \boldsymbol{u}(\boldsymbol{x}). \tag{2}$$

As is common in fluid dynamical problems, the phase space is simply the physical space corresponding to the fluid particle location.

The two terms in (1) account for (i) stretching and contraction of fluid elements owing to the straining part of the flow and (ii) the local rigid body rotation of fluid elements. Taken individually, these terms produce flows with closed streamlines. However, the two contributions, acting together, generally produce chaotic streamlines. This will be shown in §§3 and 4 where we use (1) to investigate the possible particle paths for the general class of linear external motions described above. Previously, the solution (1) has been used to study the deformation of viscous drops.

For completeness we note that the most general linear flow also includes a translational term if the drop is acted upon by an external force (e.g. gravity). In this case the drop translates at velocity $\boldsymbol{U}_{\mathrm{D}}$ in a flow with local fluid velocity $\boldsymbol{U}$. The internal velocity field then includes the contribution

$$\frac{\boldsymbol{U}-\boldsymbol{U}_{\mathrm{D}}}{2(1+\lambda)}\cdot[(2r^2-1)\boldsymbol{I}-\boldsymbol{x}\boldsymbol{x}]. \tag{3}$$

The slip velocity $\boldsymbol{U}-\boldsymbol{U}_{\mathrm{D}}$ is proportional to the density difference between the two phases:

$$\boldsymbol{U}-\boldsymbol{U}_{\mathrm{D}} = [2(1+\lambda)/(3(2+3\lambda))](\hat{\rho}-\rho)a^2\boldsymbol{g}/\mu G,$$

where the appearance of the shear rate G serves as a reminder that (3) is dimensionless. Equation (3) is the well-known Hadamard–Rybczynski solution for the internal fluid motion of a sedimenting drop.

Of course, the general situation of relative translational motion in the presence of shear, equations (1) and (3), may also be studied. However, some preliminary calculations suggest that the structure of the Poincaré sections is similar to figures 3–6 and so we have not investigated this more complicated problem further.

3. Neutrally buoyant drop in a linear flow

We consider the case of a neutrally buoyant drop in a linear flow. From the kinematical point of view it is possible to eliminate the viscosity ratio λ via a simple

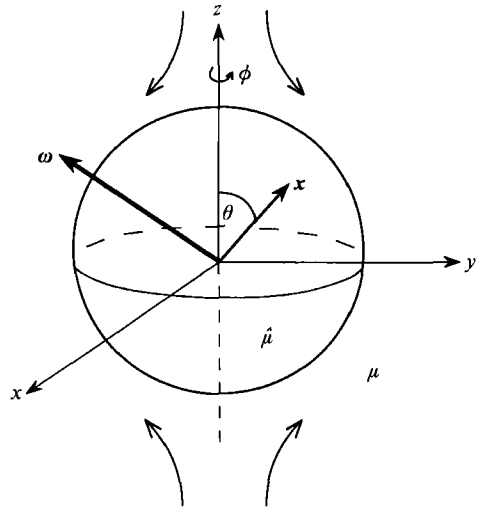

FIGURE 1. Drop in a linear flow. Coordinate system aligned with the principal axes of $\boldsymbol{E}$.

rescaling of (1). If we denote a solution of (1), corresponding to the initial condition $\boldsymbol{X}$, as $\boldsymbol{x}(t, \boldsymbol{X}; \boldsymbol{\omega}, \boldsymbol{E}, 1+\lambda)$, then we see that

$$\boldsymbol{x}(t, \boldsymbol{X}; \boldsymbol{\omega}, \boldsymbol{E}, 1+\lambda) = \boldsymbol{x}\left(t, \boldsymbol{X}; \boldsymbol{\omega}, \frac{\boldsymbol{E}}{1+\lambda}, 1\right) = \boldsymbol{x}\left(\frac{t}{1+\lambda}, \boldsymbol{X}; (1+\lambda)\,\boldsymbol{\omega}, \boldsymbol{E}, 1\right). \tag{4}$$

Hence, for any choice of viscosity ratio, the particle trajectory corresponding to a given initial condition $\boldsymbol{X}$ may be found from the $\lambda = 0$ solution to (1) by either rescaling time and the magnitude of the vorticity or, alternatively, by rescaling the rate-of-strain tensor. Physically this simple interpretation implies that an identical 'degree of mixing' (i.e. the same solution trajectory) is obtained as the viscosity of the drop phase is increased by requiring a mixing time longer by a factor of $1+\lambda$ and simultaneously changing the velocity gradient so that the vorticity is reduced relative to the rate-of-strain tensor by the factor $1+\lambda$. Therefore, for the remainder of the discussion we confine attention to the third-order dynamical system

$$\frac{\mathrm{d}\boldsymbol{x}}{\mathrm{d}t} = \tfrac{1}{2}[(5r^2-3)\,\boldsymbol{E}\cdot\boldsymbol{x} - 2\boldsymbol{x}\boldsymbol{x}\cdot\boldsymbol{E}\cdot\boldsymbol{x}] + \tfrac{1}{2}\boldsymbol{\omega}\wedge\boldsymbol{x}. \tag{5}$$

3.1. *Parameter space of the flow*

The internal flow field is specified completely by the vorticity vector $\boldsymbol{\omega}$ and the symmetric traceless rate-of-strain tensor $\boldsymbol{E}$ of the external motion. It proves convenient to choose a coordinate system specified by the principal axes of $\boldsymbol{E}$ so that

$$\boldsymbol{E} = \pm \begin{pmatrix} E_{11} & 0 & 0 \\ 0 & E_{22} & 0 \\ 0 & 0 & -(E_{11}+E_{22}) \end{pmatrix}, \tag{6}$$

where we have assumed $E_{11}, E_{22} \geqslant 0$. The external flow with inflow along the z-axis and outflow in the (x, y)-plane is shown in figure 1. Since the equations are invariant with respect to the interchanges $t \to -t$, $\boldsymbol{E} \to -\boldsymbol{E}$, and $\boldsymbol{\omega} \to -\boldsymbol{\omega}$, no generality is lost in the kinematical discussion by only focusing on the + sign in (6).

For simplicity we choose $E_{11}+E_{22}$ as the characteristic velocity and let $\alpha = E_{22}/E_{11}$. In dimensionless terms

$$\boldsymbol{E} = \begin{pmatrix} 1/(1+\alpha) & 0 & 0 \\ 0 & \alpha/(1+\alpha) & 0 \\ 0 & 0 & -1 \end{pmatrix}. \tag{7}$$

Hence, in Cartesian coordinates, the dynamical system for investigating fluid particle motion takes the dimensionless form†

$$\frac{\mathrm{d}x}{\mathrm{d}t} = \frac{1}{2}\left[(5r^2-3)\frac{x}{1+\alpha} - 2x\left(\frac{x^2}{1+\alpha}+\frac{\alpha y^2}{1+\alpha}-z^2\right)\right] + \tfrac{1}{2}(\omega_y z - \omega_z y), \tag{8a}$$

$$\frac{\mathrm{d}y}{\mathrm{d}t} = \frac{1}{2}\left[(5r^2-3)\frac{\alpha y}{1+\alpha} - 2y\left(\frac{x^2}{1+\alpha}+\frac{\alpha y^2}{1+\alpha}-z^2\right)\right] + \tfrac{1}{2}(\omega_z x - \omega_x z), \tag{8b}$$

$$\frac{\mathrm{d}z}{\mathrm{d}t} = \frac{1}{2}\left[-(5r^2-3)z - 2z\left(\frac{x^2}{1+\alpha}+\frac{\alpha y^2}{1+\alpha}-z^2\right)\right] + \tfrac{1}{2}(\omega_x y - \omega_y x). \tag{8c}$$

The parameter space to be studied can be reduced by noting that (8*a–c*) are invariant with respect to several variable transformations:

(i) The equations are invariant with respect to

$$x \to y, \quad y \to x, \quad \alpha \to 1/\alpha, \quad \boldsymbol{\omega} = (\omega_x, \omega_y, \omega_z) \to (-\omega_y, -\omega_x, -\omega_z).$$

Hence, no generality is lost in restricting $0 \leqslant \alpha \leqslant 1$.

(ii) The equations are invariant with respect to

$$x \to -x, \quad \omega_y \to -\omega_y, \quad \omega_z \to -\omega_z.$$

Hence, it is sufficient to restrict attention to $\omega_z \geqslant 0$.

(iii) The equations are invariant with respect to

$$z \to -z, \quad \omega_x \to -\omega_x, \quad \omega_y \to -\omega_y.$$

Hence, it is sufficient to study $\omega_y \geqslant 0$.

We note that the special case of simple shear flow corresponds to $\alpha = 0$, $\boldsymbol{\omega} = (0, \omega, 0)$. One can show that in this case (8*a–c*) are completely integrable. Hence this highly symmetric velocity field has a very simple, non-chaotic streamline structure.

It is also necessary to specify three parameters describing the orientation of the three orthogonal principal axes of $\boldsymbol{E}$. However, this relative orientation is only important for non-spherical shapes and, since here we are only concerned with spherical drops, it is sufficient to suppress dependence on the orientation parameters (Batchelor 1979).

It is now clear that the flow is completely specified by four parameters: α and three components of $\boldsymbol{\omega}$, with the restrictions discussed above. There are perhaps other useful representations of the flow possible, but the above description has proven to be convenient for our presentation and discussion.

† Equations with a similar cubic nonlinearity have been investigated in the context of electromagnetic stirring (Moffatt 1991).

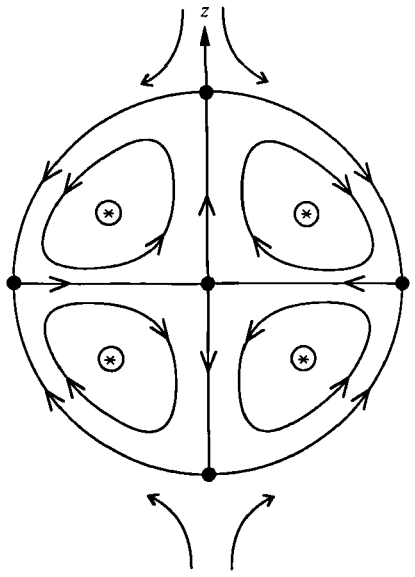

FIGURE 2. Streamlines inside the drop, $\omega = 0$. The streamsurfaces form a nested family of tori, shown here in cross-section. The filled circles denote saddle fixed points and the asterisks denote elliptic fixed points.

3.2. *Geometry of the flow*

In this paper we will study chaotic streamlines for the specific case of $\alpha = 1$, (axisymmetric $\boldsymbol{E}$). To develop intuition about the geometry of the flow, we discuss three cases: (i) $\boldsymbol{\omega} = 0$; (ii) $\boldsymbol{\omega}$ aligned along the z-axis; and (iii) $\boldsymbol{\omega}$ oriented off the z-axis.

If $\boldsymbol{\omega} = 0$, the overall flow is axisymmetric and a stream function ψ exists. In spherical coordinates (r, θ, ϕ) the stream function is given by

$$\psi(r, \theta) = \tfrac{3}{4} r^3 (r^2 - 1) \sin^2 \theta \cos \theta. \tag{9}$$

The internal streamlines for this flow are sketched in figure 2. The streamsurfaces, ψ = constant, form a nested family of tori. Particles move along closed paths in cross-sectional planes of constant ϕ. A circle of elliptic fixed (stagnation) points lies at the centre of the nest, here denoted by *. This elliptic stagnation circle plays a prominent role in the averaging calculation presented in §4.2.

For the case where the vorticity vector $\boldsymbol{\omega}$ is aligned along the z-axis, the streamsurfaces ψ = constant are still given by (9). However, the particle paths now evolve according to $\phi(t) = \omega t + \phi_0$ and so may densely cover a streamsurface, depending on the magnitude of the vorticity.

The flow becomes much more complicated when $\boldsymbol{\omega}$ is off the z-axis. It is only in this case that chaotic streamlines can occur. We will explore this both numerically and analytically in §4.

The underlying cause of the chaos can be traced back to geometric structures present in figure 2, the case $\boldsymbol{\omega} = 0$. In the language of dynamical systems theory, there is a saddle fixed point at the origin (this is a stagnation point of the flow). The poles are also saddle fixed points. In addition, there is a ring of saddle fixed points along the equator. A very important role is played by trajectories that connect saddle points; such trajectories are known as heteroclinic orbits. For example, in figure 2, heteroclinic orbits connect the origin to the pole, the pole to the equator, and

the equator back to the origin. Taken together these heteroclinic orbits form a *heteroclinic cycle*. Perturbations of such cycles provide a classic mechanism for the generation of chaos (Wiggins 1988); this appears to be the case when $\boldsymbol{\omega}$ is off the z-axis.

In the numerical investigation presented below, the effects of changing both the orientation and the magnitude of $\boldsymbol{\omega}$ will be studied independently. Because $\alpha = 1$ corresponds to an axisymmetric flow, we will take $\boldsymbol{\omega} = (\omega_x, 0, \omega_z)$ without loss of generality. The orientation of $\boldsymbol{\omega}$, measured from the z-axis in the (x, z)-plane, will be denoted by Θ.

The particle paths are computed by numerically solving (8) using both a fourth-order Runge–Kutta method and the Bulirsch–Stoer method (Press *et al.* 1986). All calculations are performed using double precision and the numerical integrations are checked by comparing the two methods and by decreasing the time-step.

To describe the three-dimensional particle paths we present Poincaré sections through the distinguished plane in the flow, namely the (x, z)-plane containing the z-axis and $\boldsymbol{\omega}$. In this case, when $\boldsymbol{\omega} = 0, \boldsymbol{E} \neq 0$, closed streamlines lie in the plane; if $\boldsymbol{E} = 0, \boldsymbol{\omega} \neq 0$, closed circular streamlines intersect the Poincaré section in exactly two points (we are counting intersections from both sides of the plane). Other plane sections yield similar qualitative behaviour. Note that Poincaré sections provide only a qualitative characterization of the flow; in particular, they provide no indication of the actual time evolution of a passive tracer in the flow.

4. Results and discussion

4.1. *Numerical results*

We begin by examining the case $\Theta = 0.275\pi$ and $|\boldsymbol{\omega}| = 1.5$ illustrated in figure 3. Most of the Poincaré section is covered by a single trajectory whose initial condition is near the origin. This trajectory corresponds to a chaotic streamline. There are also four large island structures, which occur in pairs, since they are actually cross-sections of toroidal flow regions (one pair is labelled A). To probe the structure of the unlabelled pair of islands, we use four different initial conditions inside the island. The trajectories appear as concentric curves in figure 3(*a*).

A more detailed view of an island is shown in figure 3(*b*). Particle paths which begin in the island region remain there for all time and typically remain on a toroidal surface, as suggested by the Poincaré section. The pattern is relatively simple near the centre of the island, but begins to break down as the chaotic region is approached, leading to a highly structured region of intertwined islands. The phase portrait exhibits KAM behaviour familiar from the theory of nearly integrable Hamiltonian systems (Lichtenberg & Lieberman 1983; Ottino 1989).

Notice that there is a sparse diagonal strip in figure 3(*a*). This sparseness is easily explained since the strip is aligned along the vorticity vector. For any point $\boldsymbol{x}$ parallel to $\boldsymbol{\omega}, \boldsymbol{\omega} \wedge \boldsymbol{x} = 0$, so the flow is entirely due to $\boldsymbol{E}$. Flow due to $\boldsymbol{E}$ only generates motion *in* the Poincaré plane and not transverse to the plane. Hence, whenever a typical trajectory finds itself in the neighbourhood of $\boldsymbol{\omega}$, it has a very small velocity component transverse to the plane, and therefore rarely intersects the strip. The same phenomenon has been discussed by Dombre *et al.* (1986).

The particle paths that begin near the origin in figure 3 sample a large fraction of the sphere volume. The chaotic character of this motion may be verified by demonstrating the sensitive dependence on initial conditions, manifested by exponential divergence of nearby trajectories. We have performed these standard

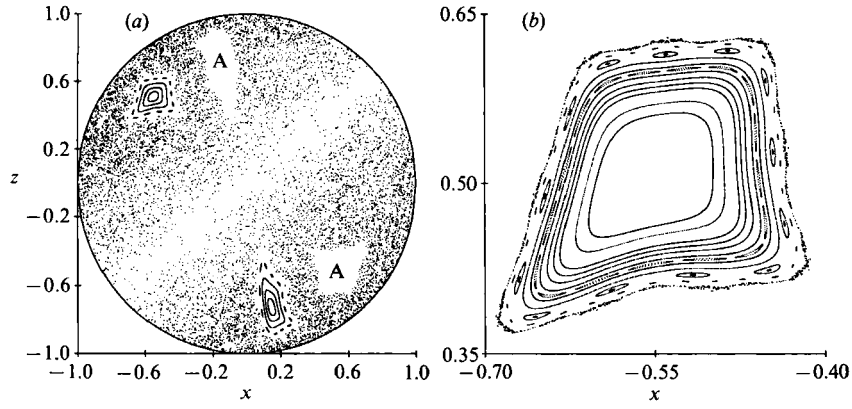

FIGURE 3. A typical Poincaré section, $|\omega| = 1.5, \Theta = 0.275\pi$. (*a*) A single chaotic trajectory with initial condition near the origin covers most of the section. The symbol A labels one pair of islands belonging to the same torus. The inner structure of the unlabelled pair of islands is also shown. (*b*) Detailed structure of one of the islands.

calculations and found that there is a continual exponential separation of two nearby particles, characteristic of a chaotic dynamical system, until the upper bound of the drop diameter is reached.

We next examine the Poincaré section for a fixed orientation of the vorticity vector, but an increasing magnitude of the vorticity. Figure 4 shows simulations for an orientation $0.2\pi = 36°$ from the z-axis. In each Poincaré section, a single particle trajectory, with initial condition near the saddle point at the origin, samples a large portion of the plane. In a few of the figures, the structure internal to the islands is shown also. For small magnitudes of ω (figure 4*a*, *b*) the streamline pattern has four large island regions similar to figure 3. As the magnitude of ω increases towards $O(1)$, islands are created and destroyed until at $|\omega| = 1.4$ a single streamline appears to fill much of the Poincaré plane. Further increases in $|\omega|$ lead to very complicated patterns filled with intertwining islands and chaotic regions, and the chaotic regions become progressively smaller with further increases in the magnitude of ω.

We now study the dependence of the Poincaré sections on the vorticity orientation Θ. Figure 5 shows the case where the magnitude of the vorticity vector is small, $|\omega| = 0.1$. Figure 5(*a*) illustrates that for Θ near zero (orientations almost vertical), the chaotic particle paths are confined to very narrow regions about the z-axis, the surface and the equator. As Θ is increased, the chaotic region increases monotonically and the islands shrink. As the orientation approaches and then exceeds $\Theta \approx 0.3\pi$ (figure 5*g*, *h*) the streamline is able to sample almost the entire cross-sectional plane and so practically fills the entire volume of the drop. We have been careful to say 'practically' since, strictly speaking, we cannot exclude the presence of stable periodic orbits with very high period. The islands corresponding to such orbits would have very small cross-section and hence would be hard to detect. Thus, we will confine our discussion to the 'dominant islands' in the Poincaré section.

Using the *method of averaging* in the limit of $|\omega| \ll 1$, it is possible to develop a good qualitative and quantitative understanding of the streamline structure illustrated in figure 5. Specifically we find that the critical orientation for the destruction of the dominant island is given by $\Theta = \cot^{-1} 1/\sqrt{2} = 0.304\pi$. This analysis is presented in §4.2.

An important qualitative feature of figure 5 is the appearance of chaotic

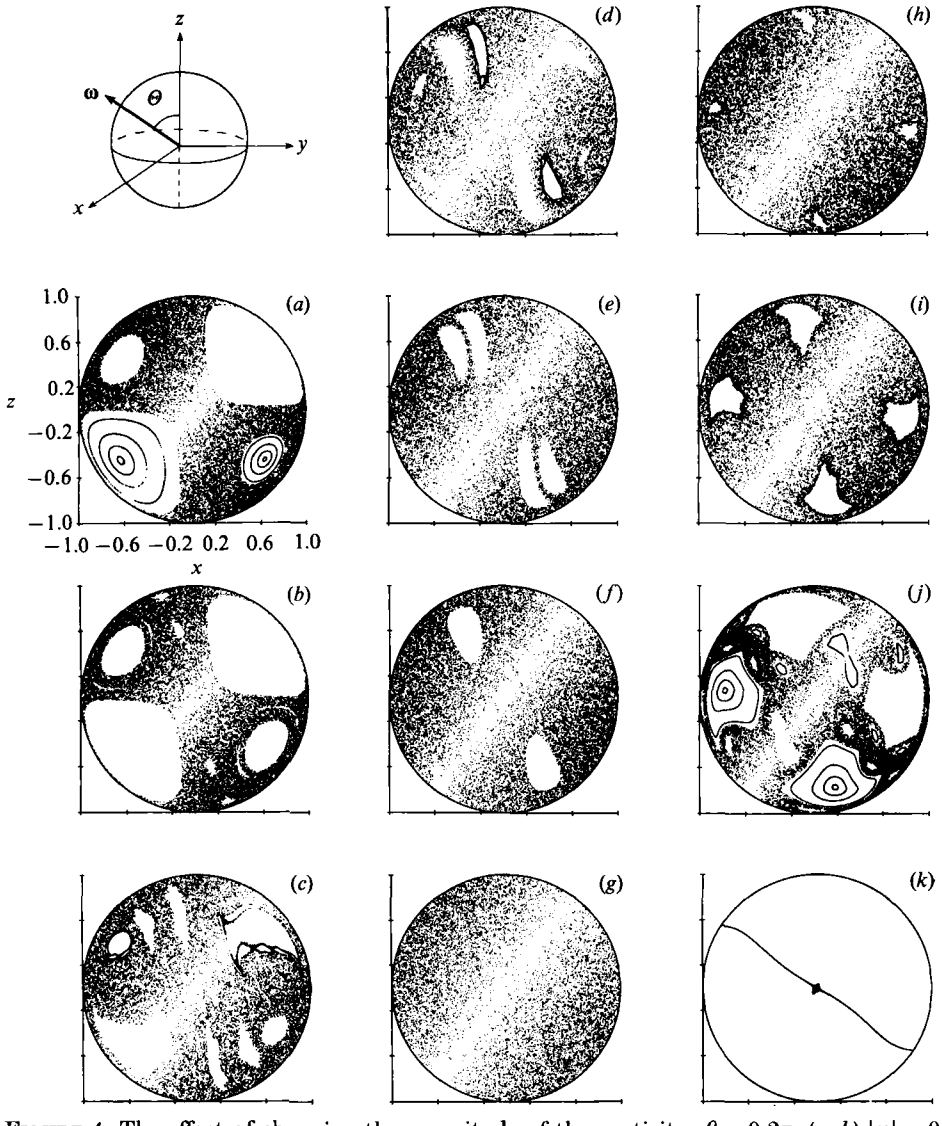

FIGURE 4. The effect of changing the magnitude of the vorticity, $\theta = 0.2\pi$. (*a–k*) $|\omega| = 0.1$, 0.5, 1.0, 1.13, 1.17, 1.25, 1.4, 1.75, 2.5, 4.0, 8.0 respectively.

trajectories for small magnitudes of vorticity, even at orientations almost, though not exactly, aligned along the z-axis (figure 5*a–c*). The existence of the chaotic trajectories is a consequence of the heteroclinic cycle carrying particles away from the origin and then back to the neighbourhood of the origin. As mentioned above, perturbations of heteroclinic cycles, here due to off-axis vorticity, are ideal candidates for generating chaos (Wiggins 1988).

For larger magnitudes of the vorticity vector, the streamline structure is modified, actually becoming qualitatively much more complex. In figure 6 we present results of changing the orientation of the vorticity vector for $|\omega| = 2$. In figure 6(*a*, *d*, *e*, *l*) we also show the inner structure of the islands. Once again, for orientations almost aligned with the z-axis, the particle paths are confined to the regions close to the z-axis, the surface and the equator (figure 6*a*, *b*). However, in figure 6(*c*), for $\Theta =$

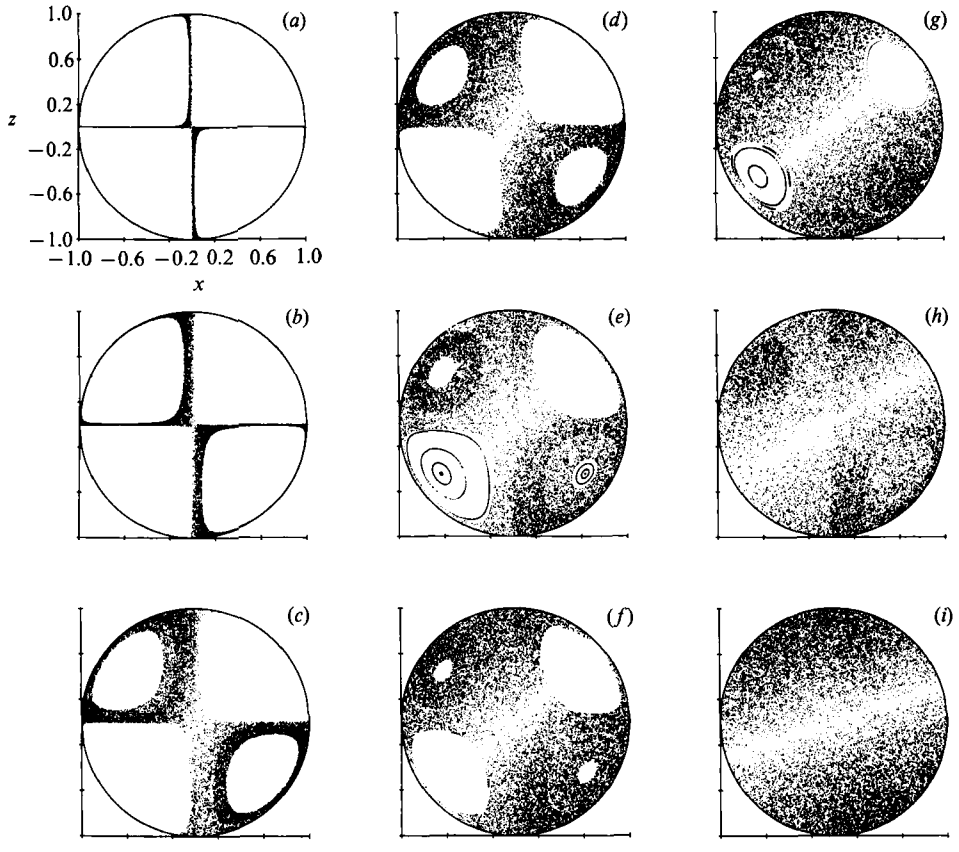

FIGURE 5. The effect of changing the orientation of the vorticity vector, $|\omega| = 0.1$. $(a$–$i)$ $\Theta = 0.001\pi$, 0.01π, 0.1π, 0.17π, 0.25π, 0.27π, 0.29π, 0.333π, 0.4π respectively.

0.0067π, we see that a bifurcation has already occurred so that a streamline which begins near the origin is able to penetrate, and thus break, part of the island structure. A series of bifurcations then continues to occur as the orientation is increased further until the particle path samples almost the entire Poincaré plane at an orientation $\Theta = 0.1\pi$ (figure 6g). Further increases in Θ lead to a complicated phase portrait with many subregions which are connected by toroidal substructures. This is vividly illustrated in figure 6(l).

4.2. *Analytical study of small* $|\omega|$ *via the method of averaging*

In this section we apply the method of averaging to understand the phase portrait in the limit of small $|\omega|$. Numerical results for $|\omega| = 0.1$ were shown in figure 5.

As discussed in §3.2, when $\omega \equiv 0$ the particle paths may be described in spherical coordinates by a stream function $\psi(r, \theta)$. Then, motion is confined to the intersection of planes ϕ = constant and toroidal surfaces ψ = constant. However, when $|\omega| \ll 1$ a fluid particle executes a slow winding motion about the z-axis and simultaneously may cross onto surfaces specified by different values of ψ. In such instances it is convenient to specify the particle location inside the spherical drop by the three independent variables $\psi(t)$, $\theta(t)$ and $\phi(t)$. It follows that for $|\omega| \ll 1$ the variables ϕ and ψ vary slowly as a function of time while θ varies rapidly. The method of averaging (Sanders & Verhulst 1985) may be used to examine the evolution of the

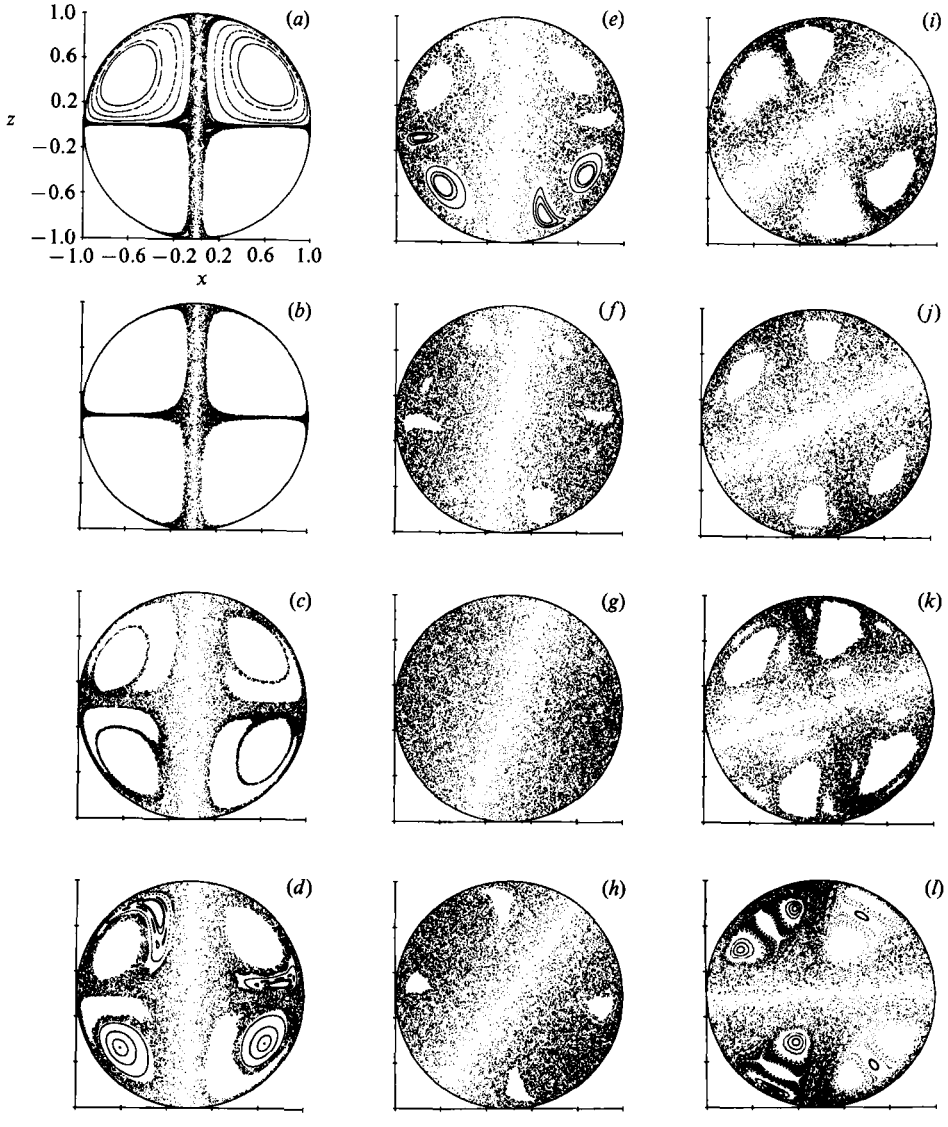

FIGURE 6. The effect of changing the orientation of the vorticity vector, $|\omega| = 2.0$. (*a–l*) $\Theta = 0.001\pi$, 0.002π, 0.0067π, 0.01π, 0.02π, 0.06π, 0.1π, 0.2π, 0.3π, 0.35π, 0.4π, 0.48π respectively.

particle path in terms of the two slow variables ψ, ϕ. As we illustrate below, the averaging calculation predicts the orientation of ω at which the islands are destroyed and predicts the approximate size of the islands shown in figure 5.

We consider the case $|\omega| \ll 1$ by perturbing the equations of motion about the elliptic stagnation circle of the $\omega = 0$ motion (see asterisks in figure 2). This choice is natural because the stagnation circle is at the centre of the toroidal islands shown in figure 5; in a qualitative sense, the neighbourhood of the stagnation circle is the most regular region of the flow and the farthest from the chaos.

The derivation of the averaged equations is given in Appendix B. Here we simply begin with the averaged equations, which are two coupled equations describing the evolution of the particle path in terms of the averaged variables ψ and ϕ. (As is

common in averaging calculations, we use the same symbol for a quantity and its average.) Instead of ψ, however, it is convenient to introduce the new variable χ, which is zero at the location of the elliptic stagnation circle and measures the distance, in terms of the stream function, from the stagnation circle. The largest value of χ is $\chi = 1$ which occurs on the z-axis, the surface and the equator. The averaged equations have the form

$$\frac{d\chi}{d\tau} = \frac{\sqrt{2}}{4}\chi(\chi-1)\sin\phi, \tag{10a}$$

$$\frac{d\phi}{d\tau} = \frac{1}{2}\left[\beta - \frac{\cos\phi}{\sqrt{2}} - \frac{1}{8\sqrt{2}}\chi\cos\phi\right], \tag{10b}$$

where $0 \leqslant \chi \leqslant 1$, $-\pi \leqslant \phi \leqslant \pi$ and the slow time $\tau = \omega_x t$. Here we have also defined the orientation parameter as $\beta = \omega_z/\omega_x = \cot\Theta$.

Now we analyse the phase portrait for the averaged system (10), as a function of the orientation parameter β. Since χ is a real number and ϕ is an angle, it is most natural to use a cylindrical phase space, with χ increasing along the length of the cylinder and ϕ increasing around it. We will plot the phase portrait for all values of χ between 0 and 1, although the picture is expected to be strictly valid only for χ near 0, since a perturbation expansion about $\chi = 0$ was used to derive the averaged equations. (For example, an unphysical feature of the averaged equation (10*a*, *b*) is the prediction of a source and sink on $\chi = 1$, whereas the actual flow is incompressible.)

The averaged system (10) has a very important symmetry: the equations are invariant under the transformation $\tau \to -\tau, \phi \to -\phi$. This means that (10) is an example of a 'reversible' dynamical system (Tsang *et al.* 1991). Such systems are known to have many special properties; in particular they have much in common with Hamiltonian systems. As will be seen below, reversibility imparts a symmetrical appearance to the phase portraits: the upper half of each figure is the same as the lower half, but with all arrows reversed (see figure 7).

Figure 7 (*a*) shows the phase portrait for $\frac{9}{8}\sqrt{2} > \beta > \beta_{\text{crit}} = 1/\sqrt{2}$. There are three fixed points: a saddle point at $\chi = 8(\sqrt{2}\beta - 1)$, $\phi = 0$ (denoted by $\oplus$), and a stable and unstable fixed point on the circle $\chi = 1$. Furthermore, the circle $\chi = 0$ is a closed trajectory. The most important feature in figure 7 (*a*) is a homoclinic orbit that leaves the saddle point $\oplus$, flows towards $\chi = 0$, loops around the back of the cylinder, and then returns to the saddle. Using the reversibility symmetry, one can prove that this homoclinic orbit traps a band of closed orbits between itself and $\chi = 0$. In particular, any trajectory which starts near $\chi = 0$ is confined to that vicinity for all time.

To interpret these results physically, recall that $\chi = 0$ corresponds to the central stagnation circle inside the toroidal streamsurfaces of figure 2. Thus, the band of trapped orbits in figure 7 (*a*) corresponds to a tube of particle paths that remain near the stagnation circle forever. In other words, figure 7 (*a*) provides a simple theoretical explanation of the ordered island regions in the original flow.

In contrast, trajectories starting outside the homoclinic orbit in figure 7 (*a*) may move towards it initially, but eventually are sent back out to large values of $\chi \approx 1$. Physically this means that the corresponding particle paths move away from the ordered region and towards the drop surface or equatorial plane. In the unaveraged flow, such large excursions are associated with chaotic streamlines.

As β approaches β_{crit} from above (Θ moves from the z-axis towards the equator),

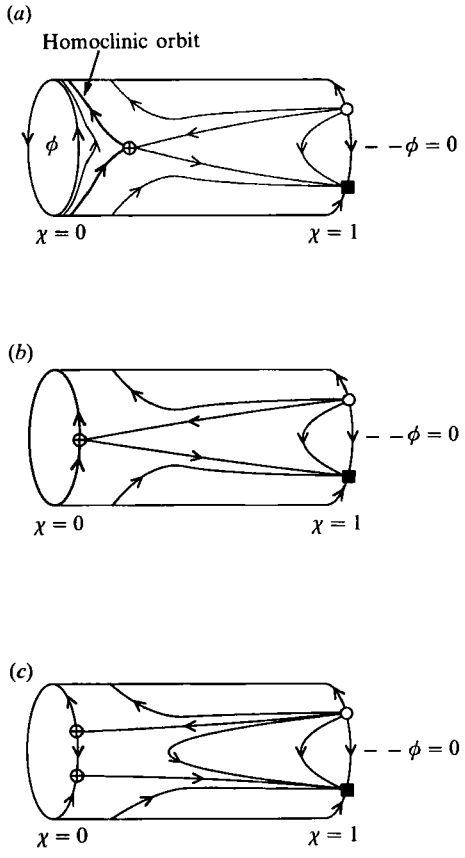

FIGURE 7. The cylindrical phase portraits corresponding to the averaged system of equations. (*a*) $\frac{2}{3}\sqrt{2} > \beta > \beta_{\text{crit}} = 1/\sqrt{2}$, (*b*) $\beta = \beta_{\text{crit}} = 1/\sqrt{2}$, (*c*) $\beta < \beta_{\text{crit}}$.

the homoclinic orbit tightens like a noose around the circle $\chi = 0$. Physically this means that the ordered region in the flow shrinks to zero. Figure 7 (*b*) shows the phase portrait at $\beta = \beta_{\text{crit}} = 1/\sqrt{2}$. The saddle point now occurs on the circle $\chi = 0$, and there is no longer a region of confined trajectories. Finally, for $\beta < \beta_{\text{crit}}$ (figure 7*c*), the saddle point splits into two saddles, but the qualitative result is the same: the ordered region of figure 7 (*a*) is destroyed.

Thus, for small $|\omega|$, the method of averaging predicts that the dominant ordered region will disappear at a critical orientation $\Theta = \cot^{-1}\beta_{\text{crit}} = 0.304\pi$. This prediction agrees with the numerical results shown in figure 5.

The method of averaging also predicts the variation in thickness of the dominant toroidal structure. The homoclinic orbit in figure 7 (*a*) moves from a maximum χ of $8(\sqrt{2}\beta - 1)$ at $\phi = 0$ to values close to $\chi = 0$ at $\phi = \pi$. Physically this implies that the island region is a tube of non-uniform cross-section: it is thickest at $\phi = 0$, and narrowest at $\phi = \pi$. This prediction also agrees with the numerics. In addition, the prediction of a maximum $\chi = 8(\sqrt{2}\beta - 1)$ has been checked numerically and is in good agreement for $\beta - \beta_{\text{crit}} < 0.03$.

5. Conclusions

In summary, we have described chaotic wandering of streamlines for the simple physical flow problem of a neutrally buoyant spherical drop in linear external Stokes flows. The kinematics are dictated completely by the magnitude of the vorticity vector and the orientation of the vorticity relative to the principal axes of the rate-of-strain tensor $\boldsymbol{E}$. The viscosity ratio of the two fluids plays no direct role. In the limit of small $|\boldsymbol{\omega}|$ the method of averaging predicts both the size of the dominant islands and the onset of chaos. Several interesting questions remain, including the study of non-axisymmetric $\boldsymbol{E}, \alpha \neq 1$, and implications of the chaotic particle paths for transport enhancement.

H.A.S. and S.H.S. gratefully acknowledge the National Science Foundation for support through Presidential Young Investigator Awards. Also we acknowledge support from NSF grant DMS-8916267 (S.H.S.) and the Petroleum Research Fund (H.A.S.).

Appendix A. A brief derivation of the Stokes velocity fields

In this Appendix we present a brief derivation of the equations describing the motion of a spherical drop in a linear velocity field at low Reynolds numbers. The dimensionless governing equations for the velocity and pressure fields $(\boldsymbol{u}^{\mathrm{e}}, p^{\mathrm{e}})$ in the external suspending fluid and in the drop fluid $(\boldsymbol{u}, p)$ are

$$\nabla^2 \boldsymbol{u}^{\mathrm{e}} = \nabla p^{e}, \quad \nabla^2 \boldsymbol{u} = \nabla p, \quad \nabla \cdot \boldsymbol{u}^{\mathrm{e}} = 0, \quad \nabla \cdot \boldsymbol{u} = 0. \tag{A 1}$$

Assuming that the drop remains nearly spherical, the boundary conditions of continuity of velocity and tangential stress are applied on the undeformed spherical surface and may be written

$$\boldsymbol{u}^{\mathrm{e}}(\boldsymbol{x}) = \boldsymbol{u}(\boldsymbol{x}) \quad \text{on} \quad r = 1, \tag{A 2a}$$

$$\boldsymbol{t} \cdot (\boldsymbol{n} \cdot \boldsymbol{T}^{\mathrm{e}} - \lambda \boldsymbol{n} \cdot \boldsymbol{T}) = 0 \quad \text{on} \quad r = 1, \tag{A 2b}$$

where $\boldsymbol{T}$ is the stress tensor, $\boldsymbol{T} = -p\boldsymbol{I} + \nabla \boldsymbol{u} + (\nabla \boldsymbol{u})^{\mathrm{T}}$, and $\boldsymbol{n}, \boldsymbol{t}$ are the unit normal and tangent vectors to the interface. The normal stress balance is not imposed here since the drop shape is taken to be spherical. However, the small shape distortions generated by viscous stresses may be calculated using the normal stress balance once the velocity and pressure fields are known. Far from the drop the flow tends to the undisturbed motion $\boldsymbol{u}^{\mathrm{e}} \to \boldsymbol{u}^{\infty}(\boldsymbol{x}) = \boldsymbol{U} - \boldsymbol{U}_{\mathrm{D}} + \frac{1}{2}\boldsymbol{\omega} \wedge \boldsymbol{x} + \boldsymbol{E} \cdot \boldsymbol{x}$, where $\boldsymbol{U}$ is the undisturbed velocity at the centre of the drop and $\boldsymbol{U}_{\mathrm{D}}$ is the translational velocity of the drop. Because of the linearity of the spherical drop problem, the solutions corresponding to the forcings $\boldsymbol{U} - \boldsymbol{U}_{\mathrm{D}}$, $\boldsymbol{\omega}$ and $\boldsymbol{E}$ may be studied independently and then superposed.

There are several methods for representing the solutions to Stokes flow problems with spherical geometries in terms of spherical harmonic eigenfunction expansions. In our work we have found an invariant vector method described by Hinch (1988) to provide a compact and very useful representation for the velocity fields. A detailed example illustrating the vector invariant solution method, closely related to the problem studied in this paper, is described by Nadim & Stone (1991) in the study of particle and drop motion in a quadratic undisturbed velocity field.

The solution for the external and internal velocity fields in the case of a translating drop in a quiescent fluid $(\boldsymbol{U} - \boldsymbol{U}_{\mathrm{D}} \neq 0, \boldsymbol{\omega} = 0, \boldsymbol{E} = 0)$ is given by Batchelor (1967). For the case of a neutrally buoyant drop, which is the primary interest in this paper, the

drop moves with the local fluid $\boldsymbol{U} = \boldsymbol{U}_{\mathrm{D}}$, so that the velocity fields internal and external to the drop depend linearly on $\boldsymbol{\omega}$ and $\boldsymbol{E}$. In this case, the velocity and pressure fields may be written

$$\boldsymbol{u}^{\mathrm{e}}(\boldsymbol{x}) = \tfrac{1}{2}\boldsymbol{\omega}\wedge\boldsymbol{x} + \boldsymbol{E}\cdot\boldsymbol{x} + c_1^{\mathrm{e}}\frac{\boldsymbol{\omega}\wedge\boldsymbol{x}}{r^3} + c_2^{\mathrm{e}}\left(\frac{2\boldsymbol{E}\cdot\boldsymbol{x}}{r^5} - \frac{5\boldsymbol{x}\cdot\boldsymbol{E}\cdot\boldsymbol{x}\boldsymbol{x}}{r^7}\right) - 3c_3^{\mathrm{e}}\frac{\boldsymbol{x}\cdot\boldsymbol{E}\cdot\boldsymbol{x}\boldsymbol{x}}{r^5}, \quad (\mathrm{A}\ 3a)$$

$$p^{\mathrm{e}}(\boldsymbol{x}) = p_\infty - 6c_3^{\mathrm{e}}\frac{\boldsymbol{x}\cdot\boldsymbol{E}\cdot\boldsymbol{x}}{r^5}; \quad (\mathrm{A}\ 3b)$$

and

$$\boldsymbol{u}(\boldsymbol{x}) = c_1\,\boldsymbol{\omega}\wedge\boldsymbol{x} + 2c_2\,\boldsymbol{E}\cdot\boldsymbol{x} + 6c_3(5r^2\boldsymbol{E}\cdot\boldsymbol{x} - 2\boldsymbol{x}\cdot\boldsymbol{E}\cdot\boldsymbol{x}\boldsymbol{x}), \quad (\mathrm{A}\ 4a)$$

$$p(\boldsymbol{x}) = p_0 + 126c_3\,\boldsymbol{x}\cdot\boldsymbol{E}\cdot\boldsymbol{x}. \quad (\mathrm{A}\ 4b)$$

The reference pressures p_∞ and p_0 differ owing to interfacial tension. The six unknown constants $c_1^{\mathrm{e}}, c_2^{\mathrm{e}}, c_3^{\mathrm{e}}, c_1, c_2, c_3$ are determined by applying the boundary conditions (A 2). After some algebra, one finds

$$c_1^{\mathrm{e}} = 0, \quad c_2^{\mathrm{e}} = -\frac{\lambda}{2(1+\lambda)}, \quad c_3^{\mathrm{e}} = \frac{2+5\lambda}{6(1+\lambda)}, \quad (\mathrm{A}\ 5a)$$

$$c_1 = \tfrac{1}{2}, \quad c_2 = -\frac{3}{4(1+\lambda)}, \quad c_3 = \frac{1}{12(1+\lambda)}. \quad (\mathrm{A}\ 5b)$$

Substitution of these results into (A 4*a*) yields (1), which is the starting point for much of the work discussed in this paper.

Appendix B. The averaging calculation for small $|\omega|$

In this Appendix we describe the application of the method of averaging to the dynamical system (8). The analysis assumes that the magnitude of the vorticity is small. A detailed derivation is given of the equations presented in §4.2. This application of averaging is in the same spirit as that described by Bajer & Moffatt (1990), though the simplicity of the equations here allows for more analytical progress.

It is natural to use spherical polar coordinates (r, θ, ϕ) to follow the motion of a fluid particle. Equations (8) may then be written

$$\frac{\mathrm{d}r}{\mathrm{d}t} = \tfrac{3}{4}r(r^2-1)(1-3\cos^2\theta), \quad (\mathrm{B}\ 1a)$$

$$\frac{\mathrm{d}\theta}{\mathrm{d}t} = \tfrac{3}{4}(5r^2-3)\sin\theta\cos\theta - \tfrac{1}{2}\omega_x\sin\phi, \quad (\mathrm{B}\ 1b)$$

$$\frac{\mathrm{d}\phi}{\mathrm{d}t} = \frac{1}{2}\left[\omega_z - \omega_x\frac{\cos\theta}{\sin\theta}\cos\phi\right]. \quad (\mathrm{B}\ 1c)$$

It is convenient here to use the stream function $\psi(r,\theta) = \tfrac{3}{4}r^3(r^2-1)\cos\theta\sin^2\theta$, as a dependent variable instead of the radial coordinate r. Although a stream function only exists in the case of zero vorticity or the special case of the vorticity vector aligned along the z-axis, for more general flows ψ simply defines the streamsurface of the undisturbed motion (see figure 2) upon which a particle lies at time t. Since

$$\frac{\mathrm{d}\psi}{\mathrm{d}t} = \frac{\mathrm{d}r}{\mathrm{d}t}\frac{\partial\psi}{\partial r} + \frac{\mathrm{d}\theta}{\mathrm{d}t}\frac{\partial\psi}{\partial\theta}$$

an equation for $\mathrm{d}\psi/\mathrm{d}t$ follows from (B 1a, b). So we now consider particle trajectories $(\psi(t), \phi(t), \theta(t))$ determined by the set of equations

$$\frac{\mathrm{d}\psi}{\mathrm{d}t} = \tfrac{1}{2}\omega_x \sin\phi \left[\frac{1-3\cos^2\theta}{\cos\theta\sin\theta}\right]\psi, \tag{B 2a}$$

$$\frac{\mathrm{d}\phi}{\mathrm{d}t} = \tfrac{1}{2}\omega_x \left[\frac{\omega_z}{\omega_x} - \frac{\cos\theta}{\sin\theta}\cos\phi\right], \tag{B 2b}$$

$$\frac{\mathrm{d}\theta}{\mathrm{d}t} = \tfrac{3}{4}(5r^2-3)\sin\theta\cos\theta - \tfrac{1}{2}\omega_x \sin\phi. \tag{B 2c}$$

For small magnitudes of the vorticity $|\boldsymbol{\omega}| \ll 1$, it is clear from (B 2) that variations in θ occur on an $O(1)$ timescale, the fast time, while variations in ψ and ϕ occur over the much longer timescale $O(1/|\boldsymbol{\omega}|)$, the slow time. An approximate description of the motion may then be constructed using a multiple timescales analysis. Here we outline the first term of such a perturbation expansion. The idea is to average the original equations over the fast $O(1)$ timescale to yield a simpler set of two equations valid on the longer $O(1/|\boldsymbol{\omega}|)$ timescale where noticeable changes in ψ and ϕ occur. As is customary in this type of calculation we do not use a separate symbol for the averaged quantities. Hence, from now on ψ and ϕ denote their averaged values.

The time-averaged form of (B 2) is given by

$$\frac{\mathrm{d}\psi}{\mathrm{d}\tau} = \tfrac{1}{2}\sin\phi \left\langle\frac{1-3\cos^2\theta}{\cos\theta\sin\theta}\right\rangle\psi, \tag{B 3a}$$

$$\frac{\mathrm{d}\phi}{\mathrm{d}\tau} = \frac{1}{2}\left[\frac{\omega_z}{\omega_x} - \left\langle\frac{\cos\theta}{\sin\theta}\right\rangle\cos\phi\right], \tag{B 3b}$$

where $\tau = \omega_x t$ is the slow timescale, and the time average of a quantity h is defined as

$$\langle h\rangle(t) = \frac{1}{\mathscr{T}}\int_t^{t+\mathscr{T}} h(s)\,\mathrm{d}s, \tag{B 4}$$

where $\mathscr{T}$ is the period of the rapid θ motion evaluated in the limit $|\boldsymbol{\omega}| = 0$.

To determine the relevant time averages in (B 3), numerical calculations could be performed over typical closed orbits inside the spherical drop. However, in the zero vorticity limit there is an elliptic point, coordinates $(r_0, \theta_0) = (\sqrt{\tfrac{3}{5}}, \cos^{-1} 1/\sqrt{3})$, at the middle of the central-most torus (denoted by an asterisk in figure 2). Furthermore, as seen in figure 5, the neighbourhood of this circle of points is the last remaining island region of the flow. So, we proceed by perturbing the equations of motion about (r_0, θ_0) and then determine the motion of $\theta(t)$ in this neighbourhood. We are then able to analytically determine the time averages in (B 3).

B.1. *Perturbation expansion in the neighbourhood of the elliptic stagnation circle*

To evaluate the time averages, consider the flow in the absence of vorticity, where the particle trajectory equations are (B 1a, b) with $\boldsymbol{\omega} = 0$. These equations are solved via a perturbation expansion about (r_0, θ_0) using the Poincaré–Lindstedt technique. Measuring the displacement from the fixed point by ϵ, let

$$r(t) = r_0 + \epsilon r_1(T) + \epsilon^2 r_2(T) + \ldots, \tag{B 5a}$$

$$\theta(t) = \theta_0 + \epsilon\theta_1(T) + \epsilon^2\theta_2(T) + \ldots, \tag{B 5b}$$

with

$$T = w(\epsilon)\,t = (w_0 + \epsilon w_1 + O(\epsilon^2))\,t. \tag{B 5c}$$

Substituting into (B 1*a*, *b*) and collecting like powers of ϵ leads to

$$O(\epsilon): \quad \frac{\mathrm{d}r_1}{\mathrm{d}T} = \frac{-\sqrt{6}}{5}\theta_1, \quad \frac{\mathrm{d}\theta_1}{\mathrm{d}T} = \frac{5}{\sqrt{6}}r_1, \quad w_0 = \frac{3}{\sqrt{5}}; \tag{B 6a}$$

$$O(\epsilon^2): \quad \frac{\mathrm{d}^2\theta_2}{\mathrm{d}T^2} + \theta_2 = \frac{1}{4\sqrt{2}} - \frac{1}{\sqrt{10}}\sin 2T + \frac{5}{4\sqrt{2}}\cos 2T, \quad w_1 = 0, \tag{B 6b}$$

where w_1 is set equal to zero to eliminate secular terms. Solving these equations subject to the initial conditions $\theta(0) = \theta_0 + \epsilon$ and $r(0) = r_0$ leads to the solution

$$\theta_1(t) = \cos T, \quad r_1(t) = -\frac{\sqrt{6}}{5}\sin T, \tag{B 7a}$$

$$\theta_2(t) = \frac{1}{6\sqrt{2}}\cos T - \frac{2}{3\sqrt{10}}\sin T + \frac{1}{4\sqrt{2}} + \frac{1}{3\sqrt{10}}\sin 2T - \frac{5}{12\sqrt{2}}\cos 2T. \tag{B 7b}$$

With the approximate representation for $\theta(t)$, it is now possible to compute the time averages defined by (B 4). The period $\mathscr{T}$ of the $\theta(t)$ motion, expressed in terms of T, is $\mathscr{T} = 2\pi$. The symbolic manipulation package *Mathematica* is used to check the algebra. We find

$$\left\langle \frac{\cos\theta(t)}{\sin\theta(t)} \right\rangle = \frac{1}{\sqrt{2}} + \frac{3}{8\sqrt{2}}\epsilon^2 + O(\epsilon^3), \tag{B 8a}$$

and

$$\left\langle \frac{1 - 3\cos^2\theta(t)}{\cos\theta(t)\sin\theta(t)} \right\rangle = \frac{3\sqrt{2}}{2}\epsilon^2 + O(\epsilon^3). \tag{B 8b}$$

Finally, it is necessary to relate the perturbation parameter ϵ, measuring distance from the fixed point (r_0, θ_0), to the slow variable ψ. To see this more clearly, expand $\psi(r(t), \theta(t))$ about (r_0, θ_0). This yields

$$\psi(r(t), \theta(t)) = -\frac{3}{25\sqrt{5}}[1 - 3\epsilon^2 + O(\epsilon^3)], \tag{B 9}$$

so that at leading order, when averaging over the fast time,

$$\epsilon^2 = \frac{1}{3}\left(1 + \frac{25\sqrt{5}}{3}\psi\right). \tag{B 10}$$

Substituting (B 8) and (B 10) into (B 3) the averaged equations take the form

$$\frac{\mathrm{d}\psi}{\mathrm{d}\tau} = \frac{3\sqrt{2}}{4}\sin\phi\left[\frac{1}{3} + \frac{25\sqrt{5}}{9}\psi\right]\psi, \tag{B 11a}$$

$$\frac{\mathrm{d}\phi}{\mathrm{d}\tau} = \frac{1}{2}\left\{\beta - \left[\frac{1}{\sqrt{2}} + \frac{3}{8\sqrt{2}}\left(\frac{1}{3} + \frac{25\sqrt{5}}{9}\psi\right)\right]\cos\phi\right\}, \tag{B 11b}$$

where $\beta = \omega_z/\omega_x$. Introducing the variable $\chi = 1 + 25\sqrt{5}\psi/3$, which measures distance from the elliptic fixed point, we finally arrive at

$$\frac{\mathrm{d}\chi}{\mathrm{d}\tau} = \frac{1}{2\sqrt{2}}\chi(\chi - 1)\sin\phi, \tag{B 12a}$$

$$\frac{\mathrm{d}\phi}{\mathrm{d}\tau} = \frac{1}{2}\left[\beta - \left(\frac{1}{\sqrt{2}} + \frac{1}{8\sqrt{2}}\chi\right)\cos\phi\right]. \tag{B 12b}$$

By construction, $\chi = 0$ at the fixed point (r_0, θ_0) and $\chi = 1$ at $\psi = 0$, which corresponds to the z-axis, the drop surface and the equator. Equations (B 12) are the starting point for the analysis of the island size and the onset of chaotic particle trajectories presented in §4.2.

REFERENCES

Aref, H. 1984 Stirring by chaotic advection. *J. Fluid Mech.* **143**, 1–21.

Aref, H. & Balachandar, S. 1986 Chaotic advection in a Stokes flow. *Phys. Fluids* **29**, 3515–3521.

Bajer, K. & Moffatt, H. K. 1990 On a class of steady confined Stokes flows with chaotic streamlines. *J. Fluid Mech.* **212**, 337–363.

Batchelor, G. K. 1967 *An Introduction to Fluid Dynamics.* Cambridge University Press.

Batchelor, G. K. 1979 Mass transfer from a particle suspended in fluid with a steady linear ambient velocity distribution. *J. Fluid Mech.* **95**, 369–400.

Dombre, T., Frisch, U., Greene, J. M., Hénon, M., Mehr, A. & Soward, A. M. 1986 Chaotic streamlines in the ABC flow. *J. Fluid Mech.* **167**, 353–391.

Hinch, E. J. 1988 Hydrodynamics at low Reynolds numbers. In *Disorder and Mixing* (ed. E. Guyon, J. P. Nadal & Y. Pomeau). NATO ASI Series, Series E, vol. 152, pp. 43–55.

Leong, C. W. & Ottino, J. M. 1989 Experiments on mixing due to chaotic advection in a cavity. *J. Fluid Mech.* **209**, 463–499.

Lichtenberg, A. J. & Lieberman, M. A. 1983 *Regular and Stochastic Motion.* Springer.

Moffatt, H. K. 1991 Electromagnetic stirring. *Phys. Fluids* A **3**, 1336–1343.

Nadim, A. & Stone, H. A. 1991 The motion of small particles and droplets in quadratic flows. *Stud. Appl. Maths* **85**, 53–73.

Ottino, J. M. 1989 *The Kinematics of Mixing: Stretching, Chaos, and Transport.* Cambridge University Press.

Press, W. H., Flannery, B. P., Teukolsky, S. A. & Vetterling, W. T. 1986 *Numerical Recipes.* Cambridge University Press.

Rom-Kedar, V., Leonard, A. & Wiggins, S. 1990 An analytical study of transport, mixing and chaos in an unsteady vortical flow. *J. Fluid Mech.* **214**, 347–394.

Sanders, J. A. & Verhulst, F. 1985 *Averaging Methods in Nonlinear Dynamical Systems.* Springer.

Swanson, P. D. & Ottino, J. M. 1990 A comparative computational and experimental study of chaotic mixing of viscous fluids. *J. Fluid Mech.* **213**, 227–249.

Tsang, K. Y., Mirollo, R. E., Strogatz, S. H. & Wiesenfeld, K. 1991 Dynamics of a globally coupled oscillator array. *Physica* D**48**, 102–112.

Wiggins, S. 1988 *Global Bifurcations and Chaos.* Springer.